Phase separation within NiSiN coatings during reactive HiPIMS discharges: A new pathway to grow Ni x Si nanocrystals composites at low temperature

J. Keraudy, R.D. Boyd, T. Shimizu, U. Helmersson, P.-Y. Jouan

Phase separation within NiSiN coatings during reactive HiPIMS discharges: a new pathway to grow Ni_xSi nanocrystals composites at low temperature

J. Keraudy[1,a)], R. D. Boyd[1], T. Shimizu[1,2], U. Helmersson[1] and P-Y. Jouan[3]

[1] *Plasma & Coatings Physics Division, IFM Materials Physics, Linköping University, SE-581 83 Linköping, Sweden*

[2] *Division of Intelligent Mechanical Systems, Graduate School of System Design, Tokyo Metropolitan University, 6-6, Asahigaoka, Hino-shi, 191-0065 Tokyo, Japan*

[3] *Institut des Matériaux Jean Rouxel (IMN), Université de Nantes, CNRS, 2 rue de la Houssinière, BP32229, 44322 Nantes cedex 3, France*

[a)] corresponding author e-mail: julien.keraudy@liu.se

Abstract

The precise control of the growth nanostructured thin films at low temperature is critical for the continued development of microelectronic enabled devices. In this study, nanocomposite Ni-Si-N thin films were deposited at low temperature by reactive high-power impulse magnetron sputtering. A composite Ni-Si target (15 at.% Si) in combination with a Ar/N_2 plasma were used to deposit films onto Si(001) substrates, without any additional substrate heating or any post-annealing. The films microstructure changes from a polycrystalline to nanocomposite structure when the nitrogen content exceeds 16 at.%. X-ray diffraction and (scanning) transmission electron microscopy analyses reveal that the microstructure consists of nanocrystals, Ni_xSi ($x > 1$) 7-8 nm in size, embedded in an amorphous SiN_x matrix. It is proposed that this nanostructure is formed at low temperatures due to the repeated-nucleation of Ni_xSi nanocrystals, the growth of which is restricted by the formation of the SiN_x phase. X-ray photoelectron spectroscopy revealed the trace presence of a ternary solid solution mainly induced by the diffusion of Ni into the SiN_x matrix. Four-probe electrical measurements reveal all the deposited films are electrically conducting.

Keywords: Silicon nitride; NiSi nanocrystals; HiPIMS; nanocomposite

Introduction

Nanocomposite thin films made from *3d* transition-metal nitride (MeN) nanocrystalline domains (up to 10 nm), randomly dispersed in an amorphous silicon nitride (*a*-SiN_x) matrix have been extensively investigated for more than two decades due to their unique physical and mechanical properties.[1–4] They exhibit high indentation hardness, excellent oxidation resistance, as well as high abrasion and erosion resistance which make

them ideal candidates for various industrial applications such as protective coatings on cutting tools, biomedical implants and decorative coatings.[5,6] The development of hard nanocomposite coatings relies on the use of a variety of transition metals with high affinity to N, such as Ti,[7–9] Cr,[10–12] Nb,[4,13,14] and Zr.[15–17] Such metals are able to form a hard and thermodynamically stable metal nitride compounds that can be used as the nanocrystalline phase. On the other hand, very few publications are devoted to the growth of SiN_x-based nanocomposite thin films with transition metal with low affinity to N, such as Fe, Cu and Ni. These transition metals can only form soft and thermodynamically metastable nitrogen-poor nitride compounds which make them unsuitable for the applications mentioned above.[18–20] However, this low affinity between metal and nitrogen can also offer the opportunity to design new nanocomposite coatings with unique functional properties.

Currently, the only low-affinity metal studied as a nanocomposite together with SiN_x, is Ni.[21–26] The $Ni_xSi_yN_z$ thin films presented in these publications consists of Si-rich nickel silicide ($NiSi_x$ with $x \geq 1$) nanocrystals (nc) encapsulated in an amorphous-SiN_x matrix. The association of $NiSi_x$-nc and a-SiN_x has been demonstrated in having a potential for applications for emerging nonvolatile memory technologies with superior retention characteristics compared to conventional floating-gate memory devices, resulting from coulomb blockade and quantum confinement effects.[21] In the references cited above, the methods of choice for the synthesis of the Ni-containing nanocomposites are reactive magnetron sputter deposition from a silicon-rich NiSi compound targets (70 at.% Si), followed by a rapid high temperature thermal annealing treatment to allow for the $NiSi_x$-nc formation. It was reported by Chen *et al.*[21,25] that the crystal growth occurred after annealing at 500-600 °C in a nitrogen atmosphere for 100 s while Huang *et al.*[22] reported growth of $NiSi_2$-nc, 4-5 nm in size, after annealing in oxygen ambient at 700 °C for 60 s. In these deposition conditions, the temperature dependence of the $NiSi_x$ crystallization is explained by the bulk diffusion and the precipitation of Ni in the amorphous nitride network.[27] Eliminating the annealing process-step, *i.e.* synthesizing as-deposited $NiSi_x$-nc through a single-step, would be beneficial for the deposition on flexible, temperature sensitive substrates, such as polymers. It would also limit the risk of oxidation and the need for a plasma cleaning step to remove any oxide layer.

In the present study, we report a straightforward strategy for that purpose, by deposition of NiSiN from a Ni-rich composite target ($Ni_{0.85}Si_{0.15}$) at different nitrogen flow rates. At a critical nitrogen flow ($N_2 \geq 6$ sccm), without the use of substrate heating or any

post-annealing, the resulting film consisted of Ni-rich Ni_xSi (x > 1)-nc, 7-8 nm in-sizes, embedded in *a*-SiN_x layer. Under these growth conditions, the formation of Ni-rich nanocrystal is driven via repeated nucleation of subsequently deposited Ni and Si atoms caused by a phase-separation mechanism taking place during the film growth.

Experimental procedures

Experiments were performed in a stainless-steel chamber (0.01 m^2) with a base pressure below 10^{-5} Pa. A $Ni_{0.85}Si_{0.15}$ composite disk with a diameter of 50 mm and a thickness of 6 mm was used as a sputtering target and mounted on a strongly unbalanced magnetron. The films were deposited onto conventional single crystal p-doped Si(001) wafers, ultrasonically cleaned in acetone then ethanol and finally dried under nitrogen flow at room temperature. The distance between the target and the substrate holder was 50 mm. Ar (sputtering gas) with a purity of 99.9997 % was introduced into the chamber through a mass flow controller with a flow rate of around 10 sccm. The reactive gas, N_2 with a purity of 99.9995 %, was introduced into the chamber with a flow rate that varied between 0 and 15 sccm. The total pressure was kept constant at 0.6 Pa by the use of a down-stream throttle valve. The average power density was kept constant at 7 W cm^{-2}, irrespectively of the reactive discharge conditions. Unipolar pulses with a length of 30 µs and a frequency of 1 kHz were supplied by a home-made high-power impulse magnetron sputtering (HiPIMS) pulsing unit fed by a Technic SR 1.5-R-1500 DC power supply. This home-made unit is also equipped with a DC current generator allowing the superposition of a low current (~ 4 mA) to produce of a low-density plasma in-between each high-power pulse ensuring a fast response-time of the discharge current.[28] The discharge current and voltage time characteristics were recorded by a Tektronix DP3014 oscilloscope using a broadband high voltage probe (Tektronix P6015) and a current probe (Tektronix TCP303), respectively, connected close to the power input to the target (see Figure.S1 of the supporting information). The applied voltage delivered to the target was varied depending on the N_2 flow rate keeping the average sputtering power constant at 100 W. High-flux, high-energy ion bombardment of the growing film was utilized with a constant substrate bias at -100 V. The film thickness was kept constant, by adjusting the deposition time, at around 1 µm independent of the N_2 flow.

The crystal structure of the films was identified by x-ray diffraction (XRD) using a Brüker D8 Advance powder diffractometer operating in Bragg-Brentano geometry (Ge monochromator $CuK_{\alpha 1}$, λ = 1.540597 Å). All XRD scans were recorded between 20 and 69°

with a step size of 0.02°. A characteristic length of the Ni nanodomains in the composite films can be extracted from the full width at half maximum of the diffraction peaks using the Scherrer formula after correction to remove the experimental broadening.[29] The chemical composition of the films was evaluated through X-ray photoemission spectroscopy (XPS) spectra recorded on a Kratos Ultra photoelectron spectrometer using a monochromatic Al Kα source (1486.6 eV) operating at 150 W. The pressure in the analysis chamber was kept below 10^{-8} Pa. A surface cleaning of Ar^+ ions impingement at 0.5 kV was applied for 15 min to remove the contaminant oxide layer (~1-5 nm) formed at the top surface by air contamination. High-resolution spectra of N *1s*, Ni *2p* and Si *2p* core levels were recorded using a pass energy of 20 eV at $\theta = 0°$ take-off angle (angle between the surface normal and the detection direction). The spectra were analyzed and fitted using the CasaXPS software.[30] A Shirley type baseline for the background and a pseudo-Voigt function with Gaussian (70%)-Lorentzian (30%) were used to fit each chemical environment composing the exposed deposited films. Finally, all spectra were calibrated in energy by using adventitious C *1s* at 284.7 eV. Scanning electron microscopy (SEM) acquisitions were carried out in a JEOL 7600F microscope with an incident electron-beam of 5 kV. The microstructure of a selected film was investigated by transmission electron microscopy (TEM). Prior to analysis, cross-sectional specimens are prepared by a two-step procedure consisting of mechanical polishing followed by Ar^+ milling at shallow incidence angle of 4° from the sample surface, with 5 keV ions initially then the ion energy was decreased to 2.5 and 1 keV. All measurements were taken with a FEI Tecnai G2 operated at 200 kV. High angle angular dark field (HAADF) and energy dispersive x-ray spectroscopy (EDS) combined with scanning-TEM (STEM) analysis were taken using a camera length of 140 mm. HAADF images were collected with the annular detector spanning an angular range from 80 to 260 mrad. The thin films' electrical resistivity was measured at room temperature using a four-point probe method in the van der Pauw configuration with a Keithley 237 current source and a Keithley 2700 multimeter. This equipment enabled the measurement of electrical resistivity below 1 x 10^5 Ω cm. The resistivity values reported in this work are average values obtained through 10 measurements.

RESULTS

In order to evaluate the impact of the addition of N_2 on the chemical composition of the coatings, XPS measurements were carried out and the results are displayed in Figure 1. For all samples, only Ni, Si and N were detected after 15 minutes of Ar^+ ion etching. These elements were quantified using the Ni *2p*, Si *2p* and N *1s* core level spectra. It was found that

increasing the N_2 flow rate in the plasma led to an increasing of the N content into the films, up to ~30 at.% whereas the Ni/Si atomic ratio stayed constant, Ni/Si ~ 6, which is close to the value of the target.

Figure 2.(a) displays XRD diffractograms of the $Ni_{1-x}Si_xN_y$ coatings with different N contents. The peaks, centered at 44.4° and 51.7° can be attributed to the (111) and (200) lattice planes of *fcc*-nickel (JCPDS: 71-4655) or of *fcc*-Ni_3Si (JCPDS: 32-700), due to the small difference in lattice parameter between Ni (3.524 Å) and Ni_3Si (3.504 Å).[31] The measured peak positions exhibit a distinct shift to higher 2θ position of both diffraction peaks with increasing N content. At the same time, the full half width maximum (FHWM) of the diffraction peaks increases and their respective intensity decreases with the N content in the film, up to a N content of 20 at.% after which the process stabilizes. Similar behavior, *e.g.* increasing of FHWM and peak intensity have been previously observed in many other sputtered transition metal carbide- and silicide-based nanocomposite systems and is commonly related to a reduction of the crystallite size.[32–35] Estimating the crystallite size using the Scherrer formula from the 111 lattice planes confirms a decrease of the grain size from 24 to 7 nm with increasing N content from 0 to 20 at.% in the coatings, see Figure 2.(b). For higher content, the crystallite size stays constant at around 7 nm.

To investigate the microstructural evolution of $Ni_{1-x}Si_xN_y$ layers with increasing N content, three selected films containing 0, 16 and 27 at.% of N were analyzed by cross-sectional bright-field TEM (BF TEM) investigations, which are shown in Figure 3. Without N, the $Ni_{1-x}Si_x$ thin film exhibits a dense columnar microstructure, as highlighted by the low-resolution micrograph (top panel, Figure 3.(a)). Such a microstructure is typical for thin films grown using HiPIMS discharges.[36] Selected-area electron diffraction (SAED) pattern (left bottom panel, Figure 3.(a)) reveals an 111-orientated *fcc* crystal texture, in good agreement with XRD results. Moreover, one can also observed the presence of a weak (211) diffraction ring between (200) and (220), which is characteristic of a Ni_3Si crystal structure. High-resolution TEM (HR-TEM) (right bottom panel Figure 3.(a)) shows consistently well-defined lattice fringes.

Upon incorporation of 16 at.% of N into the films, one can see from the bright field TEM micrograph, see Figure 3.(b), that the columnar nature still is retained. In addition, the SAED pattern is consistent with the one found at 0 at.% N film, with only an additional faint ring in the (111) position. Note that the additional (211) diffraction ring is still apparent. HR-

TEM displays both intensity variation and nanosized regions where no lattice fringes are apparent, indicating that here the structure consist of columnar grains which are sprinkled with localized amorphous regions (see, for example the black rectangle, Figure 3.(b)).

Finally, $Ni_{1-x}Si_xN_y$ coating containing 27 at.% of N displays a completely different microstructure without any trace of columnar grains (Figure 3.(c)). At high resolution, the microstructure is shown to consist of nanocrystallites randomly distributed in an apparently amorphous matrix (Figure 3.(c)), whose size is in the range of 5-7 nm, which is in good agreement with the value extracted from the XRD measurements. The presence of nc domains is further highlighted by the SAED pattern, which consists of almost continuous rings, that can be associated with a randomly orientated a *fcc*-structure and (211) Ni_3Si. Further TEM analysis was carried out on the $Ni_{1-x}Si_xN_y$ coating containing 27 at.% of N by high angle annular dark field (HAADF) STEM, shown in Figure 4.(a), which indicates that the nano-sized domains have an overall higher atomic weight (brighter) compared to the surrounding matrix (darker). The details are revealed by the overlaid colored Ni (green) and Si (red) elemental map, obtained using EDS (Figure 4.(b)), showing the heavier Ni in the domains and the lighter Si in the matrix. Due to the insensitivity of EDS to light elements a reliable N map could not be obtained. It is well-known that the presence, or not, of percolated domains may have a strong impact over the films electric conductivity, which is a crucial importance for microelectronic applications. Supporting evidence, although not conclusive, comes from a high-resolution TEM (HRTEM) micrograph (Figure 4.(c)) illustrating two possible interconnecting points between nano-sized domains. The first with partial attachment with minimal interaction between only 2-3 atomic columns (marked region #1) and second with direct attachment between two crystalline facets (marked region #2).

In order to have a deeper understanding of the chemical atomic bonds within and between the $NiSi_x$-nc and the matrix, high-resolution XPS analyses were carried out. Figure 5.(a) describes, with three representative samples, the influence of an increasing N content on the Si bond structure in the $Ni_{1-x}Si_xN_y$ coatings. To see all the collected spectra, please refer to the Figure S2 in the supporting information. Two separate features can be observed in the spectra. As the N content within the film increases, the signals of Si $2p_{3/2}$ and Si $2p_{1/2}$ are decreasing. These two peaks, located at binding energies of 99.3 and 99.7 eV, can be attributed to Si-Ni bonding.[31,37] Peaks associated to Si-N bonds, located at 100.3, 101.4 and 102 eV, appears for the film with 12 at.% N or higher, and increases with N content. According to Schmitt *et al.*,[38] the different binding energies of Si-N bonds, observed in the

spectrum, originate mainly from the different tetrahedral bond of SiN_x, *i.e.* Si-Si-N, Si-N-N, and to a smaller extent to the presence of nearest-neighbor effects (secondary chemical shifts). Figure 5.(a), reveals that the component associated with the Si-N framework increases with N content in detriment to the Si-Ni framework (please refer to the Figure S3 on the supporting information). At 27 at.% N, the relative contribution of Si-N represents ~ 40% of the total spectrum. Therefore, it is reasonable to assume that the Si-rich matrix observed in the previous TEM micrographs (see Figure 4.(b)) mainly consist of SiN_x, which is commonly observed in other silicide systems, *e.g.*, Ti-Si-N,[35] Cr-Si-N,[12] and Nb-Si-N.[4] Nonetheless, it is important to point out that the contribution of Ni-Si bonds remains the dominant one. This can be attributed to the higher Ni content compared to N in the $Ni_{1-x}Si_xN_y$ layer, as emphasized by the XPS analysis shown in Figure 1.

Regarding the Ni *2p* photoemission spectra (Figure 5.(b)), all the Ni $2p_{3/2}$ line envelope consisted of three parts: a main emission line located at 852.7 eV $\pm$ 0.2 eV followed by an asymmetric high binding energy tail at 856.0 $\pm$ 0.3 eV, and a well-resolved shake-up satellite at 858.2 $\pm$ 0.3 eV.[37,39] According to the work done by Cao *et al.*,[31] it is difficult to precisely attribute the Ni $2p_{3/2}$ main peak to the correct chemical environment of Ni atoms due to the overlap between pure Ni and Ni-rich silicide compounds (ex: Ni_3Si and $Ni_{31}Si_{12}$) peaks. In comparison to the Ni $2p_{3/2}$ peak relative to the pure Ni environment (852.7 eV), the Ni $2p_{3/2}$ core-level shift (ΔE_c) for the Ni-rich silicides compounds is ΔE_c = 0.1-0.3 eV, which is more or less the ΔE_c associated error for the charge correcting calibration using C *1s* ($\Delta E_c = \pm$ 0.2 eV).[40] This implies that a correct identification of the chemical environment of Ni atoms by investigating Ni $2p_{3/2}$ core-level spectra is not possible.

Based on the information extracted from the XPS core-level spectra analyses, TEM micrographs and EDS analyses, it can be concluded that the $Ni_{1-x}Si_xN_y$ nanocomposite thin films deposited at higher N_2 flow ($N_2 \geq 6$ sccm) are composed of randomly oriented Ni-dominated nc embedded in a-SiN_x matrix, with for the presence of Si and Ni within the nc domains and amorphous matrix respectively.

Recently, Aballe *et al.*[41] reported on the high diffusivity and chemical reactivity of Ni in the SiN_x lattice by occupying lattice interstitials leading to the formation of a localized ternary solid solution ($Ni_xSi_{1-x}N_y$), even at room temperature. To confirm the presence of this ternary alloy within the Si-rich matrix, a dealloying treatment was carried out on the nanocomposite coating with 27 at.% of N. This approach consists in a preferential etching of

the metal alloys domains by a simple treatment in a nitric acid (HNO_3), ~5 min.[42,43] In general, the dealloying process is employed to produce nanoporous materials,[44] however in this study it was used to find out the chemical constitution of the Si-rich domains. Cross-section SEM micrographs recorded on $Ni_{1-x}Si_xN_y$ with 27 at.% N before and after etching are displayed in Figure 6. After chemical etching, the film thickness was strongly reduced by 30% and become difficult to image it in the SEM, indicating a low electric conductivity of the film. Similar reduction of the film thickness was already observed by Bouts *et al.*,[44] for a Cu/C nanocomposite, and was explained by a mechanical relaxation of the material occurring as a consequence to the removal of the metal rich nanocrystals from the non-conducting matrix.

EDS compositional analysis confirmed the preferential dissolution of Ni atoms during the dealloying process in nitric acid, where after 5 min of etching the Ni:Si ratio drops from 8:1 to 1:1. Bright field TEM analysis, shown in Figure 7.(a), reveals that, after the chemical treatment, the well-defined nanocomposite structure seen previously is no longer evident. At high resolution (Figure 7.(b)), TEM analysis reveals that the Ni-rich nano-domains have been selectively etched and only weak lattice fringes (inset in the Figure 7.(b)) remain which is attributed to a residue of materials from Ni-rich nanocrystals. The low crystalline quality of the film is further confirmed by its associated fast Fourier transform (FFT) pattern (Figure 7.(c)), where very weak spots are detected. Additionally, HAAF-STEM micrograph (Figure 7.(d)) indicates that the size of the brighter nano-sized domains have significantly decrease compared to the ones observed from the film prior to treatment (Figure 4.(a)). All of which indicates the selective removal of the crystalline Ni-rich nanocrystals.

After the HNO_3 treatment, the Si *2p* core levels, see Figure 8.(a), comprises merely one component arising from Si-N bonds, and Ni-Si bonds are almost absent, confirming the preferential removal of the Ni-based NCs from the film. This result is also supported by the analysis of the Ni *2p* core levels spectra, as shown in Figure 8.(b), which after etching exhibits a weak and noisy Ni *2p* with the presence of a new peak at 855 eV. According to the literature,[21,23] this new feature can be related to the Ni-Si-N ternary bond. Thus, this additional analysis tends to reveal that the nanocomposite structure found in $Ni_{1-x}Si_xN_y$ thin films with N content higher than 16 at.% is composed of Ni-rich nanocrystals around an amorphous SiN_x with inclusions of a ternary alloy.

The electrical room-temperature resistivity of the as-deposited $Ni_{1-x}Si_xN_y$ films versus the N content is shown in the Figure 9. Without N, the value of the electrical resistivity of a 1 µm-thick $Ni_{0.83}Si_{0.14}$ film is found to be 45 µΩ cm which is higher than a pure 1-µm thick Ni layer (ρ = 13 µΩ cm) but lower than for Ni_3Si thin films that has been measured to 96 µΩ cm and to 82 µΩ cm for 150 nm and 500 nm-thick films, respectively.[45,46] As the N content increases from 2.5 to 27 at.%, an increase of the resistivity can be noticed, from 45 to 65 µΩ cm. In addition, the most significant increase in resistivity can be observed when the nitrogen content goes above 12 %, which coincide with appearance of the SiN_x phase in the Si *2p* XPS spectra (see Figure 5.(a)). This increase can be attributed to the finite size effect induced by the decreasing of the crystallite size, as emphasized by XRD analysis (see Figure 2.(b)). Nonetheless, these electrical measurements reveal that, regardless of the N content, all the NiSiN films exhibit a good electrical conductivity.

DISCUSSION

The results provided from the structural, microstructural and chemical investigations presented above clearly point out that two separated growth mechanisms take place in Ni-rich $Ni_{1-x}Si_xN_y$ thin films as a function of the N content incorporated during the film growth.

At low N content (between 0 and 16 at.%), both Ni and Si ad-atoms can diffuse on the surface of the substrate, encounter another adatom and form clusters which then serve as a sink for the subsequent stages of film growth including island nucleation and growth, impingement and coalescence of islands and development of a continuous film.[47,48] Compositional inhomogeneities within the film are unlikely due to the fact that Ni and Si are fully miscible.[49] A calorimetric investigation[50] as well as thermodynamic modeling of the Ni-Si system[51–53] report the solid solubility of Si in the *fcc* phase of Ni at about 10 at.% Si. Therefore, the slight shift to higher 2θ positions observed for all the samples (see Figure 2.(a)), *i.e.* smaller interatomic distances than in the pure Ni framework, is likely caused by the incorporation of Si atoms into the lattice, *e.g.* the Ni-Si bond distances (2.37 Å),[54] are shorter than the Ni-Ni (2.59 Å).[54] Moreover, according to the Ni-Si equilibrium phase diagram,[55] the presence of two-phase alloys α-Ni and intermetallic β-Ni_3Si or possibly a supersaturated α-$Ni_{1-x}Si_x$ solid solution can be presumed at 10-15 at.% Si, which results in a higher electrical resistivity in comparison to the pure Ni coating (see Figure 9). The columnar structure observed in the TEM micrograph (see Figure 3.(a)) is commonly seen for polycrystalline sputtered thin films deposited at low substrate temperature, according to the structure zone

model proposed by Thornton.[56] In addition, the columns and intercolumnar boundaries observed in our $Ni_{1-x}Si_xN_y$ HiPIMS films deposited at low N content are dense, due from the intense low-energy ion irradiation from Ni^+, Ar^+, Si^+ and to some extent N_2^+ and N^+ ions during the film growth. Indeed, reactive HiPIMS discharges, even in the absence of an applied substrate bias, are well-known to provide ion-assisted growth, where the deposited flux is composed to a large fraction of metal ions having an average kinetic ion energies of $\langle E_i \rangle \sim$ 15-20 eV and a neutral sputtered flux with a kinetic energy of $\langle E_n \rangle \sim 2$ eV.[57,58] The use of a continuous substrate bias, here -100V, can provide additional kinetic energy (+100 eV) to the incident ions species at the substrate surface, resulting in a higher adatom mobility during the film growth and ultimately leads to a reduction of intracolumnar as well as intercolumnar porosity, as shown by Petrov et al.[47] Under such conditions, dense $Ni_{1-x}Si_xN_y$ films can be grown even in the absence of substrate heating, which corresponds to zone 3 in the extended structure zone diagram, where energetic ion bombardment is taken into account.[59]

Films grown with very low N content, *i.e.* N < 5 at.% exhibit a strong (111) texture which is usually reported for *fcc* metallic thin film deposited on a native SiO_2 surface by magnetron sputtering since close-packed (111) planes have the lowest relative surface energy.[60] This result also demonstrates that adding 15 at.% Si in the Ni sub-lattice does not modify the film texture in comparison to pure Ni film. On the other hand, XRD analysis (see Figure 2.(a)) revealed that adding a relatively small amount of N, *i.e.* N < 10 at.%, has a strong impact on the preferred orientation of the films where a clear transition from (111) to (002) is observed. XRD patterns also revealed that both the (111) and (200) peak positions were shifted to lower diffraction angles as a result of nitrogen incorporation. No nickel nitride phase (Ni_4N, Ni_3N or Ni_2N) were detected whatever the N_2 gas flow added during the present investigation. Similar behavior, *e.g.* transition from (111) to (002) preferred orientation, has already been observed for NiN_x films deposited by conventional magnetron sputtering at different N_2 flow rate, with and without the use of substrate heating.[61–63] The exact mechanism for this orientation change is not yet fully understood, but according to Kawamura *et al.*[61] it is considered that the dominant effect controlling Ni nanostructure evolution under these growth conditions is the change in steady-state surface chemistry. The high N_2^+ ion fluxes at the substrate surface tends to increase N coverage on Ni(200) surfaces, thereby greatly decreasing the surface energy γ_{200} of the (200) plane such that $\gamma_{200} < \gamma_{111}$ and leads to the competitive evolution of (200), rather than (111) orientation. These results suggest that

one can selectively tune the preferred orientation of Ni or Ni-rich Ni_3Si films by properly adjusting a small concentration of N.

Bright field TEM micrograph analysis of the $Ni_{1-x}Si_xN_y$ coatings containing 16 at.% N (see Figure 3.(b)) reveals that the columnar structure is still preserved and composed of localized amorphous regions. Based on the XPS analysis, one can assume that these amorphous regions are SiN_x-based resulting from the higher chemical affinity of N with Si (as discussed in below) than Ni and the low solubility of SiN_x in the Ni-rich phase which induces the segregation of two-dimensional (2D) nitride layers (nitride tissue phases) to surfaces and grain boundaries of the Ni-rich Ni_3Si system. Deposition of two immiscible phases can causes strong modification of the thin film formation process, limiting grain coarsening during coalescence and film growth.[64] The resulting texture remains zone 3 with columns extending through the film, but with a lesser degree of preferred orientation and a smaller grain size as shown in Figure 2.(a) and Figure 2.(b), respectively.

At higher N content (from 16 up to 27 at.%), clear phase separation starts to occur leading to a progressive formation of a nanocomposite structure for a N content > 16 at.% (see Figure 3.(c)) with small Ni-rich nanocrystals partially surrounded by a Si-rich amorphous matrix, as seen in the cross-section TEM micrographs (Figure 4). The physical causes for the phase separation are not well understood as many processes can lead to such behavior.[65] Previous studies on the crystallization of NiSi-nc in SiN_x reported the appearance of nanocrystals under specific conditions of temperature. Under these deposition conditions, nanocrystal growth took place after a rapid thermal annealing at a temperature of ~ 600 °C during 60 seconds.[21–23,26] The average size of the nanocrystal was estimated to be between 4 and 7 nm, with the annealing temperature. In addition, the stoichiometry of all the deposited $Ni_{1-x}Si_xN_y$ films were typically Si-rich with Si content up to 70 at.%. Therefore, according to the ternary system nickel-silicon-nitrogen phase diagram proposed by Weitzer and Schuster,[66] the thermodynamically stable structure for these alloying elements would be in coexistence between a metallic phase (either elemental or intermetallic) and SiN_x. Even though, as film growth conditions during sputter depositions are far from equilibrium, a metastable solid solution phase $Ni_xSi_{1-x}N_y$ are generally reported. Chen *et al.*[21,23] presented XPS data in the form of Ni *2p* core-level spectra, where a single peak was clearly assigned to a ternary $Ni_xSi_{1-x}N_y$ solid solution nitride. Their experimental findings suggest that Ni atoms are uniformly distributed in the bulk of the amorphous network during film growth. As a results, the temperature dependence of the $NiSi_x$ crystallization under these conditions can only be

explained by bulk diffusion and precipitation of Ni in the amorphous nitride network[27] often termed "metal induced crystallization" (MIC).[67] As the temperature of the thermal annealing increases, accumulated Ni atoms bond to Si atoms and form islands, resulting in the nucleation and subsequent growth of $NiSi_x$ nanocrystal with $x > 1$.[68] The driving force for such a process is the reduction in the free energy due to amorphous-crystalline phase transformation.[69] Similar effects have been observed for the formation of $NiSi_x$ nanocrystal in amorphous silicon[68,70–72] and silicon oxide.[73,74] In the present study, the nanocrystal growth occurs in the films, without any additional substrate heating, provided that a critical amount of N_2 was added. Due to the low growth temperature, bulk diffusion can be ruled out and only surface diffusion can occur during the film growth.[75]

At the early stage of growth, both Ni and Si ad-atoms can freely diffuse on the substrate surface and form islands which then serves as a sink for the subsequently deposited Ni and Si atoms.[49,76] Since the flux of the deposited Ni atoms is higher than that of Si, the development of Ni-rich Ni_xSi ($x > 1$) islands will still be dominant. However, one must keep in mind that, in reactive sputtering conditions, N species (N ad-atoms and N_2) can also be adsorbed and diffuse on the growing film surface. Due to the higher affinity of N with Si as compared with Ni, *e.g.* the enthalpy of formation (ΔH) at room temperature for Si-N and Ni-N are ΔH = -470 and ΔH =-70-85 kJ mol^{-1},[23] respectively, will favor the formation of an amorphous SiN_x phase (see Figure 5.(a)). As the N concentration is further increased in comparison to the $Ni_{1-x}Si_xN_y$ coatings containing 16 at.% N, here the 2D SiN_x tissue phase completely covers Ni-rich islands of all orientations at the initial stage of the film growth and coarsening during coalescence is hindered. As observed from the STEM micrograph (Figure 4), the resulting film growth proceeds through repeated renucleation with clear phase separation into Ni-rich and Si-rich domains. Resulting films are composed of small Ni-rich nanocrystals with random orientation (see Figure 2.(a)) dispersed in an amorphous nitride matrix. The nanocrystal growth mechanisms suggested in the present study is consistent with most of the observations reported in the literature for nanocomposite M-Si-N systems (M = Ti, Nb, Zr, Cr) deposited at low temperature.[4] For these systems, the typical nanocomposite microstructural change appears for a Si concentration between 7 and 20 at.%, which is relatively close to our condition, ~12 at.% Si. Thus, the decreasing of the diffraction peak intensity of the Ni-rich phase (Figure 2.(a)) and the decreasing of the crystallite size from 18 to 7 nm derived from the diffraction peak widths (Figure 2.(b)) with increasing N content,

results in a broadening of the particle size distribution towards smaller dimensions due to the continuous development of the 2D SiN_x tissue phase.

Our results also demonstrate that Ni atoms can be incorporated in the Si-rich matrix during the growth, forming a ternary solid solution (see Figure 8.(b)). The Ni incorporation in the SiN_x phase can be understood in view of the high diffusivity and solubility of Ni in Si-N lattice.[77] Indeed, Ni, like Cu, belongs to the group of *3d* transition metals, which are considered as the fastest diffusers in Si at high temperature,[78] but even at room temperature.[79]

Finally, the small increase of the room temperature electrical resistivity from about 45 to 65 μΩ with increasing N content suggests that the conduction mechanism of the as-deposited coatings is not strongly affected by the transition to a nanocomposite microstructure. Similar results have been reported by Sandu *et al.*[80] for nanocomposite ZrN/SiN_x thin films deposited using bias voltages of -150 V and a substrate temperature of 250°C and, more recently, by Ramiez *et al.*[81] for N-deficient TaN/SiN_x thin films. The authors attributed the weak dependence of the electrical resistivity to the frequent percolation of the nearest-neighbors conducting crystallites due to the small coverage of the SiN_x phase. The idea of a percolation conduction path, in our films, is supported by the HRTEM analysis (see the marked region labeled #2 in the Figure 4.(e)), revealing that the surface coverage of SiN_x is too small to completely encapsulate the Ni-rich crystallites leading to the percolation of two nearest-neighbor crystallites. This percolation pathway between Ni-rich crystallites offers a highly conducting network for charge carriers to diffuse across the entire film thickness, reducing the electrical resistivity. In addition, due to the small thickness of the SiN_x layer, as emphasized by the marked region labeled #1 in the Figure 4.(e), electrical transport could also be occurred through tunneling.[81] Completely isolating the Ni-rich crystallites, and thus increase of the electrical resistivity, should be possible by increasing the Si content within the films.

CONCLUSION

In the present work, Ni-Si-N thin films were reactively deposited employing HiPIMS from a $Ni_{0.85}Si_{0.15}$ composite target at different nitrogen gas flow. By adjusting reactive gas both the N concentration, and as a direct consequence, the microstructure of the films can be controlled. A clear transition of a polycrystalline Ni-rich Ni-Si film to a nanocomposite film composed of 7-8 nm Ni-rich Ni_xSi nanocrystals embedded in an amorphous SiN_x layers was

observed when the nitrogen content reached a value above 16 at.%. The formation of Ni-rich nanocrystal is driven via repeated nucleation of subsequently deposited Ni and Si atoms caused by the phase-separation process taking place during the film growth. The proposed scenario is expected to be the same for other metals with a low affinity to nitrogen, such as Cu, Co and Fe. This single-step process provides the possibility of *in situ* fabrication of NiSi nanocrystals without any additional heating, necessary for the development of new nonvolatile nanocrystal memories deposited onto temperature-sensitive substrates.

ACKNOWLEDGMENTS

The authors would like to acknowledge H. Machhadani for helpful discussions regarding nitric acid treatment. JK acknowledges financial support from the Swedish Government Strategic Research Area in Materials Science on Functional Materials at Linköping University (Faculty Grant SFO-Mat-LiU No. 2009-00971) and the Swedish Research Council (grant VR 621-2014-4882).

REFERENCES

[1] S. Vepřek, J. Vac. Sci. Technol. Vac. Surf. Films **17**, 2401 (1999).
[2] S. Vepřek and S. Reiprich, Thin Solid Films **268**, 64 (1995).
[3] S. Veprek, J. Vac. Sci. Technol. Vac. Surf. Films **31**, 050822 (2013).
[4] C.S. Sandu, M. Benkahoul, R. Sanjinés, and F. Lévy, Surf. Coat. Technol. **201**, 2897 (2006).
[5] S. Veprek, M.G.J. Veprek-Heijman, P. Karvankova, and J. Prochazka, Thin Solid Films **476**, 1 (2005).
[6] S. Veprek and M.J.G. Veprek-Heijman, Surf. Coat. Technol. **202**, 5063 (2008).
[7] M. Diserens, J. Patscheider, and F. Lévy, Surf. Coat. Technol. **120**–**121**, 158 (1999).
[8] M. Diserens, J. Patscheider, and F. Lévy, Surf. Coat. Technol. **108**–**109**, 241 (1998).
[9] S. Hao, B. Delley, S. Veprek, and C. Stampfl, Phys. Rev. Lett. **97**, 086102 (2006).
[10] J.H. Park, W.S. Chung, Y.-R. Cho, and K.H. Kim, Surf. Coat. Technol. **188**–**189**, 425 (2004).
[11] E. Martinez, R. Sanjinés, O. Banakh, and F. Lévy, Thin Solid Films **447**, 332 (2004).
[12] D. Mercs, P. Briois, V. Demange, S. Lamy, and C. Coddet, Surf. Coat. Technol. **201**, 6970 (2007).
[13] A.D. Pogrebnjak, O.V. Bondar, G. Abadias, V. Ivashchenko, O.V. Sobol, S. Jurga, and E. Coy, Ceram. Int. **42**, 11743 (2016).
[14] M. Benkahoul, C.S. Sandu, N. Tabet, M. Parlinska-Wojtan, A. Karimi, and F. Lévy, Surf. Coat. Technol. **188**–**189**, 435 (2004).
[15] C.S. Sandu, F. Medjani, R. Sanjinés, A. Karimi, and F. Lévy, Surf. Coat. Technol. **201**, 4219 (2006).
[16] S.H. Sheng, R.F. Zhang, and S. Veprek, Acta Mater. **59**, 297 (2011).
[17] N. Ghafoor, I. Petrov, D.O. Klenov, B. Freitag, J. Jensen, J.E. Greene, L. Hultman, and M. Odén, Acta Mater. **82**, 179 (2015).
[18] J.F. Pierson, Vacuum **66**, 59 (2002).
[19] D. Vempaire, F. Fettar, L. Ortega, F. Pierre, S. Miraglia, A. Sulpice, J. Pelletier, E.K. Hlil, and D. Fruchart, J. Appl. Phys. **106**, 073911 (2009).

[20] J. -F. Bobo, H. Chatbi, M. Vergnat, L. Hennet, O. Lenoble, P. Bauer, and M. Piecuch, J. Appl. Phys. **77**, 5309 (1995).
[21] W.-R. Chen, T.-C. Chang, P.-T. Liu, J.-L. Yeh, C.-H. Tu, J.-C. Lou, C.-F. Yeh, and C.-Y. Chang, Appl. Phys. Lett. **91**, 082103 (2007).
[22] J.-J. Huang, P.-C. Yang, S.-C. Chen, H.-C. Huang, D.-S. Gan, N.-J. Ho, Y. Shi, and A.-K. Chu, Appl. Phys. Lett. **96**, 262107 (2010).
[23] W.-R. Chen, T.-C. Chang, J.-L. Yeh, S.M. Sze, and C.-Y. Chang, J. Appl. Phys. **104**, 094303 (2008).
[24] W.-R. Chen, T.-C. Chang, J.-L. Yeh, and C.-Y. Chang, J. Electrochem. Soc. **155**, H869 (2008).
[25] Y.-T. Chen, T.-C. Chang, J. Lu, J.-J. Huang, P.-C. Yang, S.-C. Chen, A.-K. Chu, H.-C. Huang, D.-S. Gan, N.-J. Ho, and Y. Shi, Thin Solid Films **518**, 7324 (2010).
[26] W.-R. Chen, T.-C. Chang, J.-L. Yeh, C.-Y. Chang, and S.-C. Chen, Appl. Phys. Lett. **92**, 062112 (2008).
[27] T.-C. Chang, F.-Y. Jian, S.-C. Chen, and Y.-T. Tsai, Mater. Today **14**, 608 (2011).
[28] J. Keraudy, B. Delfour-Peyrethon, A. Ferrec, J. Garcia Molleja, M. Richard-Plouet, C. Payen, J. Hamon, B. Corraze, A. Goullet, and P.-Y. Jouan, J. Appl. Phys. **121**, 171916 (2017).
[29] A.L. Patterson, Phys. Rev. **56**, 978 (1939).
[30] N. Fairley, Copyright© 2005 Casa Softw. Ltd (2005).
[31] Y. Cao, L. Nyborg, and U. Jelvestam, Surf. Interface Anal. **41**, 471 (2009).
[32] N. Nedfors, O. Tengstrand, E. Lewin, A. Furlan, P. Eklund, L. Hultman, and U. Jansson, Surf. Coat. Technol. **206**, 354 (2011).
[33] A. Furlan, U. Jansson, J. Lu, L. Hultman, and M. Magnuson, J. Phys. Condens. Matter **27**, 045002 (2015).
[34] J. Patscheider, T. Zehnder, and M. Diserens, Surf. Coat. Technol. **146**, 201 (2001).
[35] S. Veprek, A. Niederhofer, K. Moto, T. Bolom, H.-D. Männling, P. Nesladek, G. Dollinger, and A. Bergmaier, Surf. Coat. Technol. **133**, 152 (2000).
[36] M. Lattemann, U. Helmersson, and J.E. Greene, Thin Solid Films **518**, 5978 (2010).
[37] P.L. Tam, Y. Cao, and L. Nyborg, Surf. Sci. **606**, 329 (2012).
[38] S. Schmidt, T. Hänninen, C. Goyenola, J. Wissting, J. Jensen, L. Hultman, N. Goebbels, M. Tobler, and H. Högberg, ACS Appl. Mater. Interfaces **8**, 20385 (2016).
[39] X. Yu, X. Wang, Q. Zhang, J. Li, and J. Liu, J. Appl. Phys. **116**, 073508 (2014).
[40] D.J. Miller, M.C. Biesinger, and N.S. McIntyre, Surf. Interface Anal. **33**, 299 (2002).
[41] L. Aballe, L. Gregoratti, A. Barinov, M. Kiskinova, T. Clausen, S. Gangopadhyay, and J. Falta, Appl. Phys. Lett. **84**, 5031 (2004).
[42] H.-D. Yu, Z. Zhang, and M.-Y. Han, Small **8**, 2621 (2012).
[43] D. Wan, X. Xia, Y. Wang, and Y. Xia, Small **9**, 3111 (2013).
[44] N. Bouts, A.-A. El Mel, B. Angleraud, and P.-Y. Tessier, Carbon **83**, 250 (2015).
[45] T. Iijima, A. Nishiyama, Y. Ushiku, T. Ohguro, I. Kunishima, K. Suguro, and H. Iwai, IEEE Trans. Electron Devices **40**, 371 (1993).
[46] M. Amiotti, A. Borghesi, G. Guizzetti, and F. Nava, Phys. Rev. B **42**, 8939 (1990).
[47] I. Petrov, P.B. Barna, L. Hultman, and J.E. Greene, J. Vac. Sci. Technol. Vac. Surf. Films **21**, S117 (2003).
[48] K. Sarakinos, D. Magnfält, V. Elofsson, and B. Lü, Surf. Coat. Technol. **257**, 326 (2014).
[49] W. Tang, B.-M. Nguyen, R. Chen, and S.A. Dayeh, Semicond. Sci. Technol. **29**, 054004 (2014).
[50] P. Knauth, A. Charaï, and P. Gas, Scr. Metall. Mater. **28**, 325 (1993).
[51] Y. Du and J.C. Schuster, Metall. Mater. Trans. A **30**, 2409 (1999).
[52] T. Tokunaga, K. Hashima, H. Ohtani, and M. Hasebe, Mater. Trans. **45**, 1507 (2004).
[53] D. Connétable and O. Thomas, J. Alloys Compd. **509**, 2639 (2011).

[54] S. Gruner, J. Marczinke, L. Hennet, W. Hoyer, and G.J. Cuello, J. Phys. Condens. Matter **21**, 385403 (2009).
[55] S.G.T. Europe (SGTE), in *Ternary Steel Syst. Phase Diagr. Phase Transit. Data* (Springer, Berlin, Heidelberg, 2012), pp. 55–55.
[56] J.A. Thornton, J. Vac. Sci. Technol. **11**, 666 (1974).
[57] F. Cemin, D. Lundin, C. Furgeaud, A. Michel, G. Amiard, T. Minea, and G. Abadias, Sci. Rep. **7**, 1655 (2017).
[58] A. Ferrec, J. Keraudy, S. Jacq, F. Schuster, P.-Y. Jouan, and M.A. Djouadi, Surf. Coat. Technol. **250**, 52 (2014).
[59] A. Anders, Thin Solid Films **518**, 4087 (2010).
[60] A.J. Francis and P.A. Salvador, J. Mater. Res. **22**, 89 (2007).
[61] M. Kawamura, K. Iibuchi, Y. Abe, and K. Sasaki, Jpn. J. Appl. Phys. **43**, 4361 (2004).
[62] M. Kawamura, Y. Abe, and K. Sasaki, 6 (2000).
[63] N. Popović, ž. Bogdanov, B. Goncić, S. Štrbac, and Z. Rakočević, Appl. Surf. Sci. **255**, 4027 (2009).
[64] E. Lewin, D. Loch, A. Montagne, A.P. Ehiasarian, and J. Patscheider, Surf. Coat. Technol. **232**, 680 (2013).
[65] A.A. El Mel, N. Bouts, E. Grigore, E. Gautron, A. Granier, B. Angleraud, and P.Y. Tessier, J. Appl. Phys. **111**, 114309 (2012).
[66] F. Weitzer and J.C. Schuster, J. Solid State Chem. **70**, 178 (1987).
[67] S.Y. Yoon, K.H. Kim, C.O. Kim, J.Y. Oh, and J. Jang, J. Appl. Phys. **82**, 5865 (1997).
[68] F.A. Ferri, A.R. Zanatta, and I. Chambouleyron, J. Appl. Phys. **100**, 094311 (2006).
[69] R.B. Iverson and R. Reif, J. Appl. Phys. **62**, 1675 (1987).
[70] F.A. Ferri and A.R. Zanatta, J. Appl. Phys. **104**, 013534 (2008).
[71] A.R. Zanatta and F.A. Ferri, J. Appl. Phys. **102**, 043509 (2007).
[72] A.R. Zanatta, D.C. Ingram, and M.E. Kordesch, J. Appl. Phys. **116**, 123508 (2014).
[73] W.-R. Chen, T.-C. Chang, J.-L. Yeh, S.M. Sze, and C.-Y. Chang, Appl. Phys. Lett. **92**, 152114 (2008).
[74] J. Ren, B. Li, J.-G. Zheng, and J. Liu, Solid-State Electron. **67**, 23 (2012).
[75] M. Berndt, G. Abrasonis, G.J. Kovács, M. Krause, F. Munnik, R. Heller, A. Kolitsch, and W. Möller, J. Appl. Phys. **109**, 063503 (2011).
[76] A. Alberti and A. La Magna, J. Appl. Phys. **114**, 121301 (2013).
[77] E.R. Weber, Appl. Phys. A **30**, 1 (1983).
[78] J. Lindroos, D.P. Fenning, D.J. Backlund, E. Verlage, A. Gorgulla, S.K. Estreicher, H. Savin, and T. Buonassisi, J. Appl. Phys. **113**, 204906 (2013).
[79] N. Yarykin and J. Weber, Appl. Phys. Lett. **109**, 102101 (2016).
[80] C.S. Sandu, N. Cusnir, D. Oezer, R. Sanjinés, and J. Patscheider, Surf. Coat. Technol. **204**, 969 (2009).
[81] G. Ramírez, D. Oezer, M. Rivera, S.E. Rodil, and R. Sanjinés, Thin Solid Films **558**, 104 (2014).

Figure caption:

Figure 1. Evolution of the element concentration into $Ni_{1-x}Si_xN_y$ layers determined through XPS measurements as a function of the nitrogen flow rate. All the analyses were performed after an *in situ* cleaning of the surface using an Ar ion gun operating at 0.5 keV.

Figure 2. (a) X-ray diffraction patterns and (b) crystallite size dependence estimated from the 111 diffraction peak with the Scherrer equation for NiSiN coatings with different N content on Si(001) at room temperature.

Figure 3. Cross-sectional transmission electron microscopy (TEM) analysis of the $Ni_{1-x}Si_xN_y$ thin films containing 0 at.% (a), 16 at.% (b) and (c) 27 at.% of N. The top panels are bright-field TEM micrographs from the thin films along with their respective SAED patterns, left bottom panels, fitted to a *fcc*-structure. Note the presence of a very weak (211) diffraction ring between (200) and (220), which is characteristic of a Ni_3Si crystal structure. The right bottom panels are high-resolution TEM (HR-TEM) micrographs of a defined region of the microstructure.

Figure 4. Advanced microscopy characterization of the $Ni_{1-x}Si_xN_y$ thin film containing 27 at.% of N. HAADF-STEM image (a), the corresponding EDS-STEM map (b), with green indicating Ni and red indicating Si, of the same area and HR-TEM image of a single crystallite (c) with two regions indicating possible interconnection to other domains either by three atomic columns (region #1) or direct attachment (region #2).

Figure 5. High-resolution XPS core level spectra of the Si *2p* (a) and Ni *2p* (b) region for $Ni_{1-x}Si_xN_y$ coatings containing 0, 16 and 27 at.% N. The spectra were acquired after Ar^+ sputter cleaning.

Figure 6. Cross-sectional SEM micrographs of the $Ni_{1-x}Si_xN_y$ film containing 27 at.% of N before etching (a) and after treatment in nitric acid for 5 min.

Figure 7. Cross-sectional TEM micrographs of $Ni_{1-x}Si_xN_y$ film containing 27 at.% of N recorded after chemical etching in nitric acid for 5 min. (a) Bright field TEM micrographs at low (a) and high magnification (b), its associated FFT pattern (c), and an additional HAADF-STEM micrograph (d). Inset in (b) highlights one of the weak lattice fringes observed in the etched sample.

Figure 8. XPS core level spectra of the Si *2p* (a) and Ni *2p* (b) region for $Ni_{1-x}Si_xN_y$ coatings containing 27 at.% N before and after nitric etching. The spectra were acquired after Ar^+ sputter cleaning.

Figure 9. Room-temperature electrical resistivity of the $Ni_{1-x}Si_xN_y$ thin films as a function of the N content.

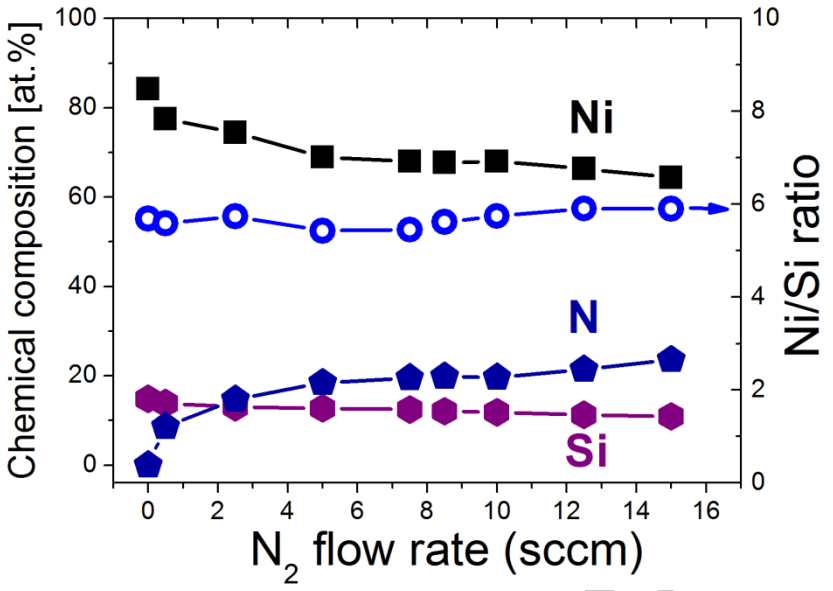

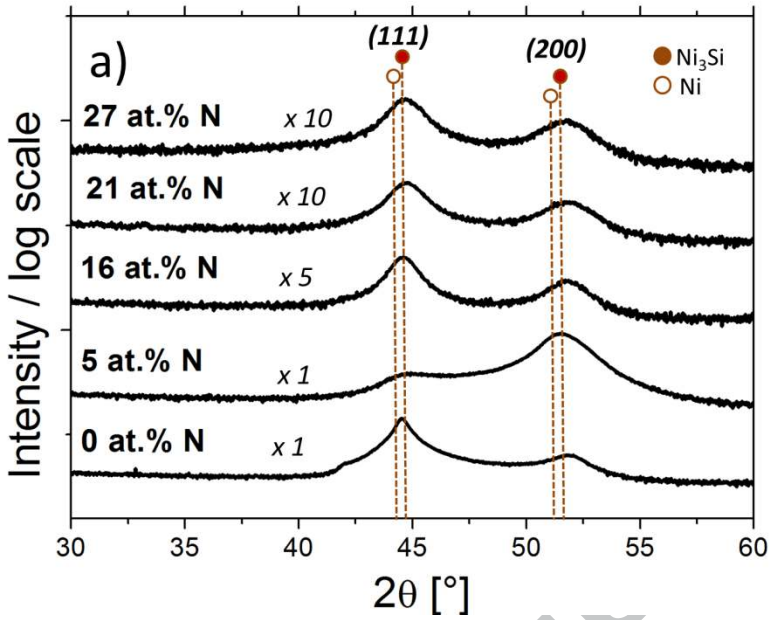

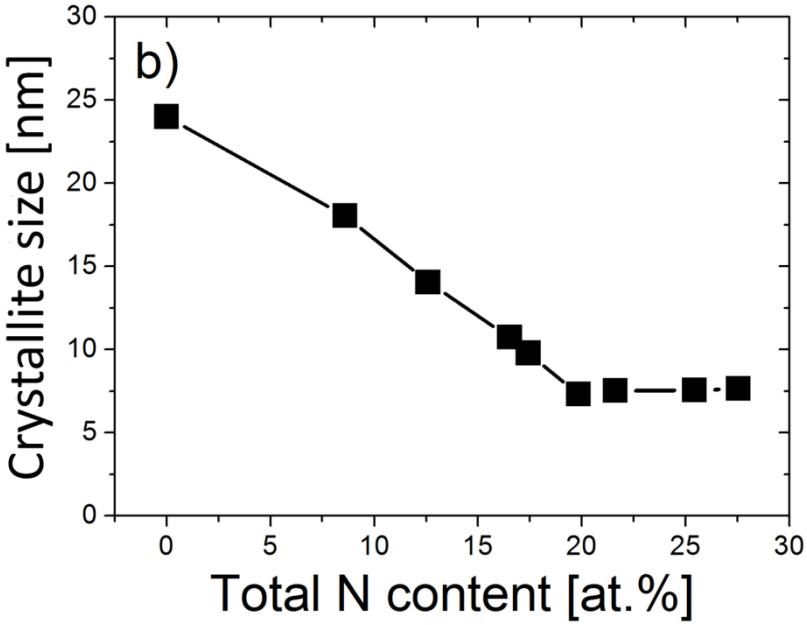

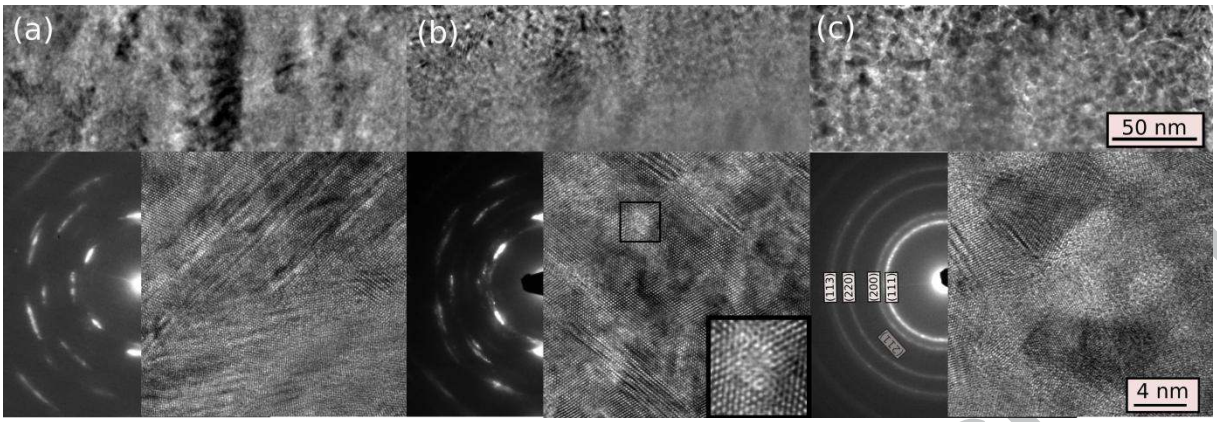

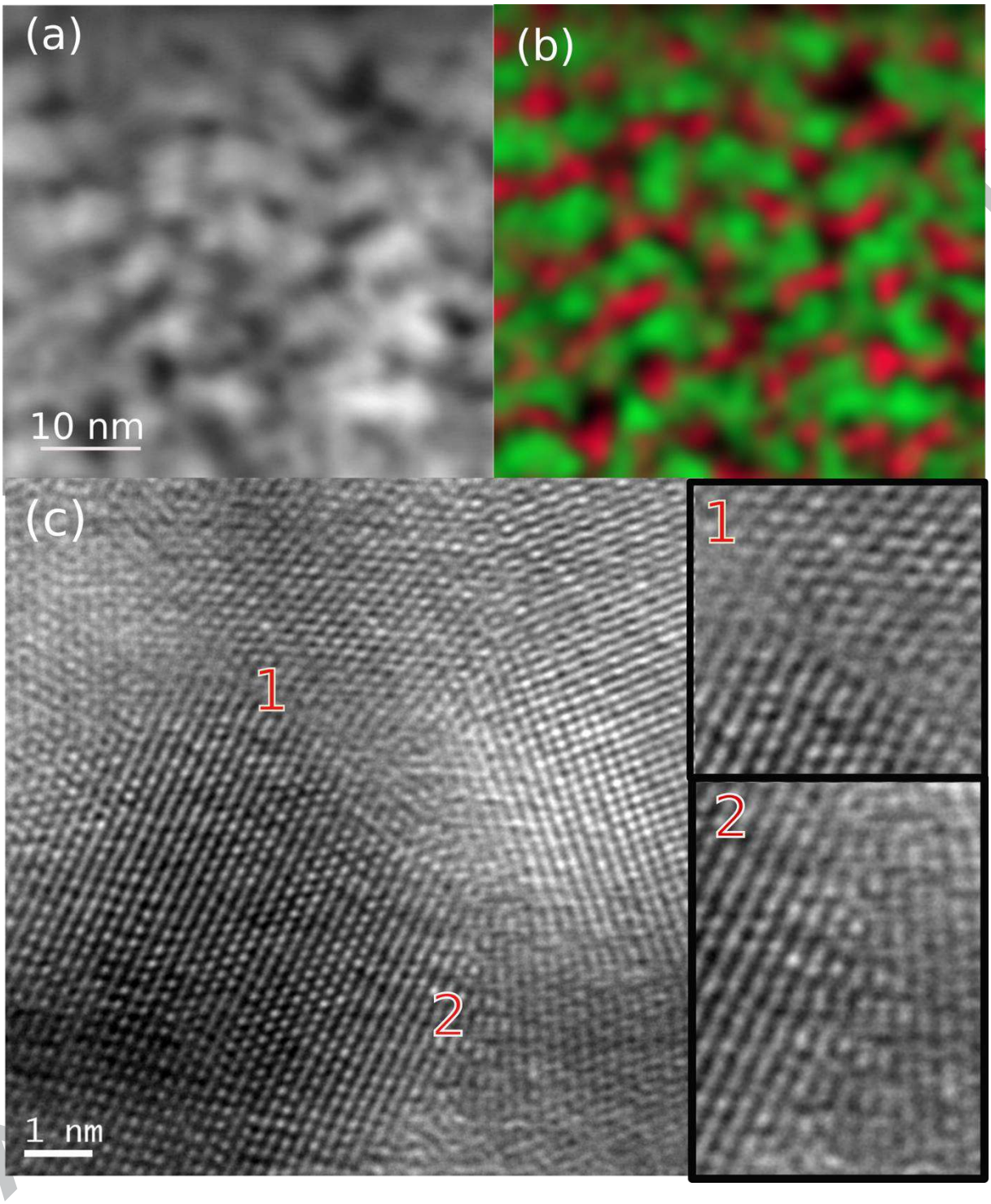

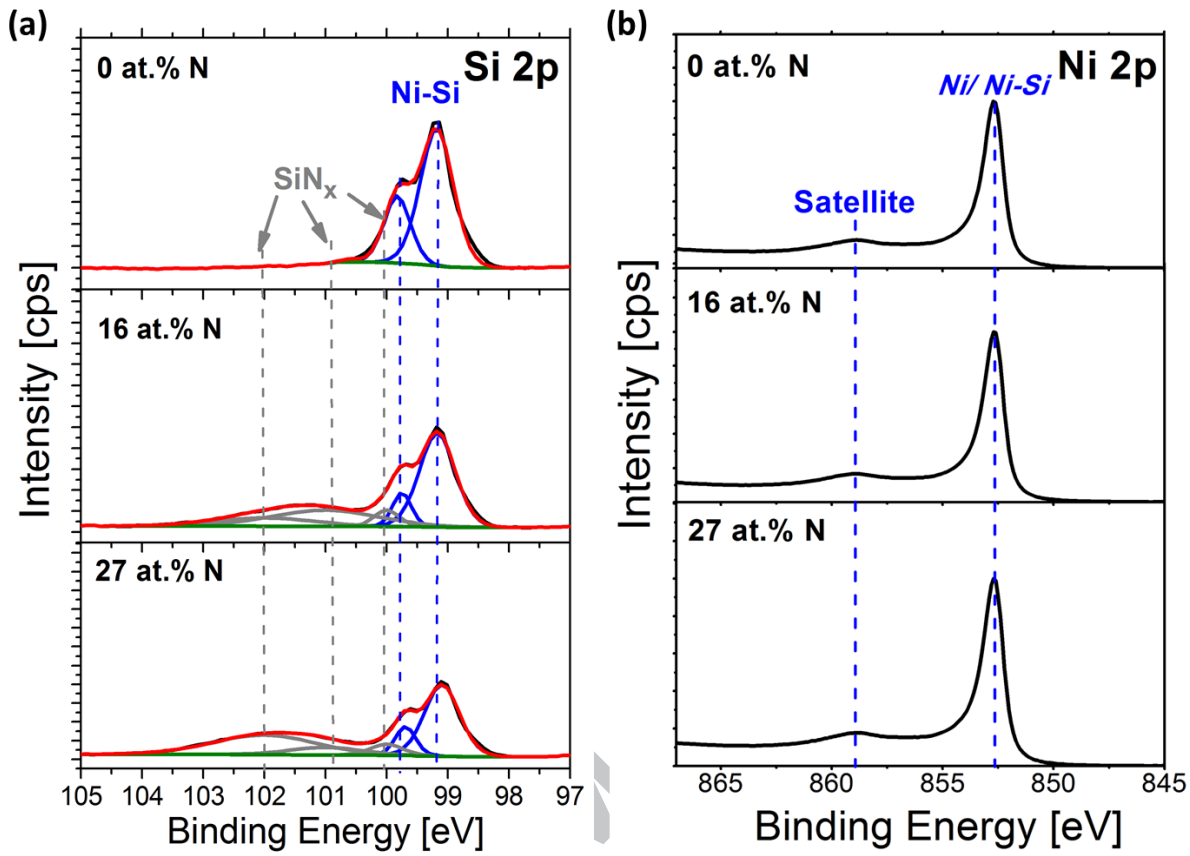

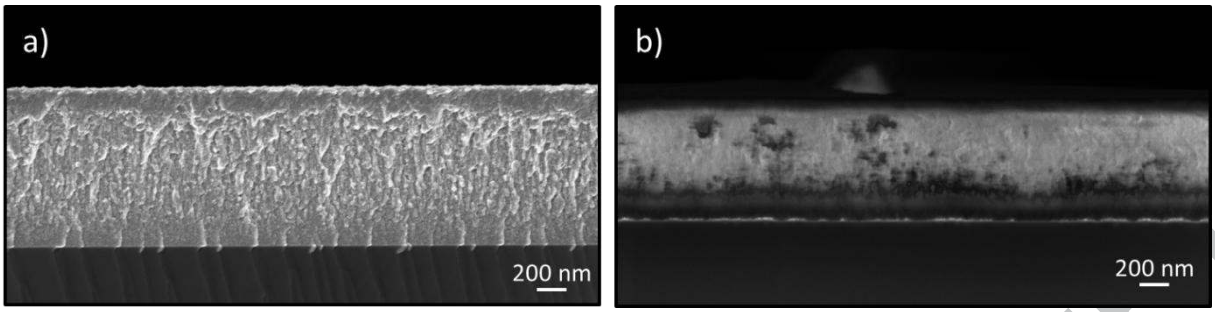

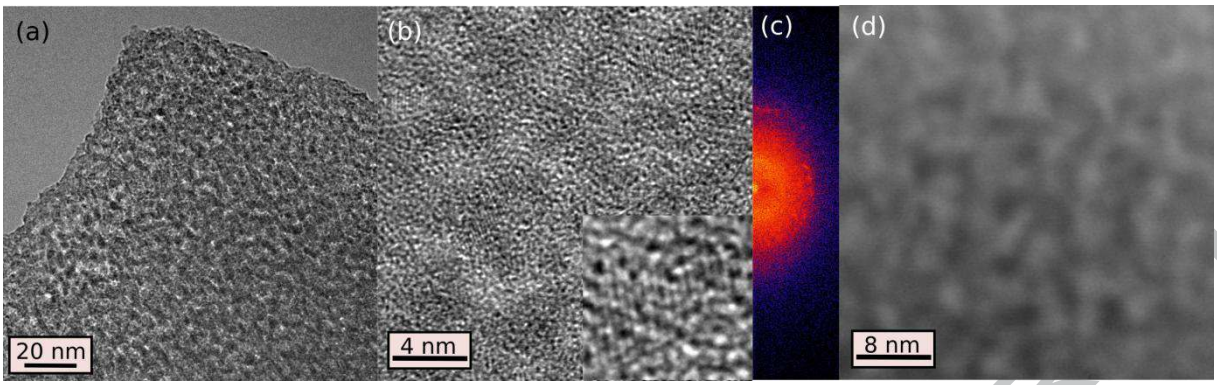

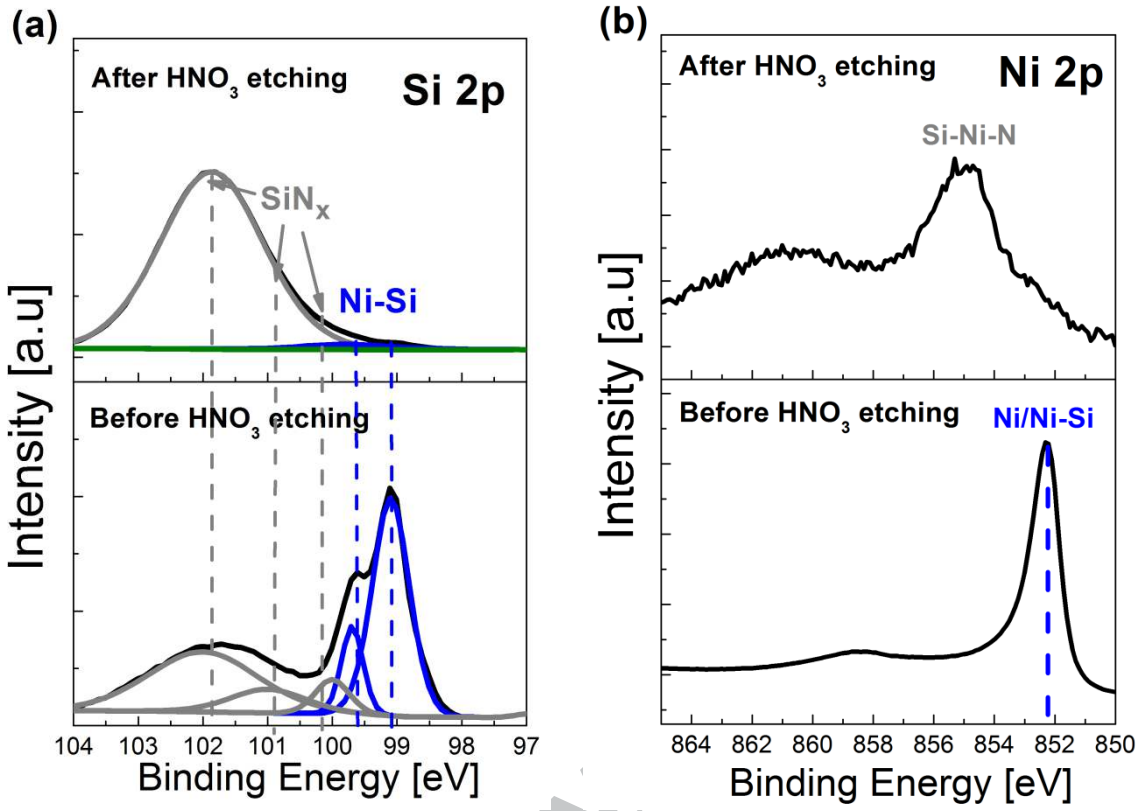

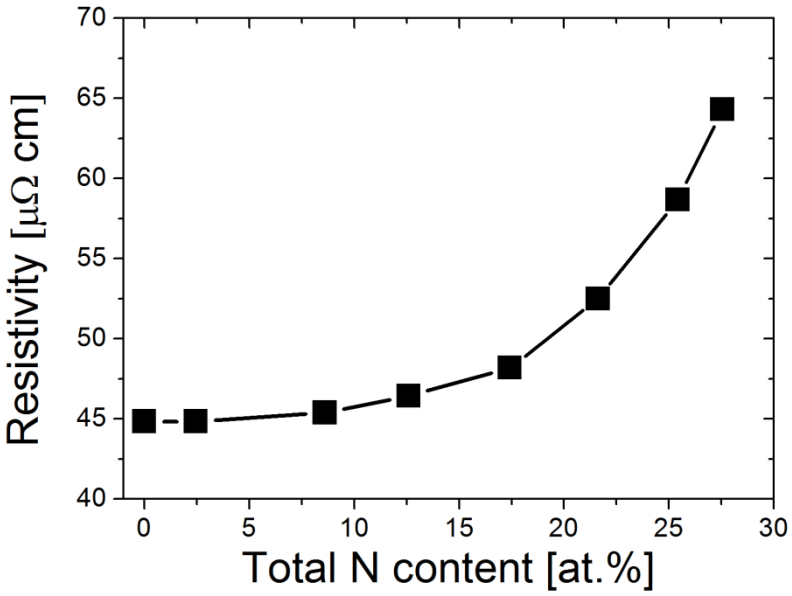

Graphical abstract

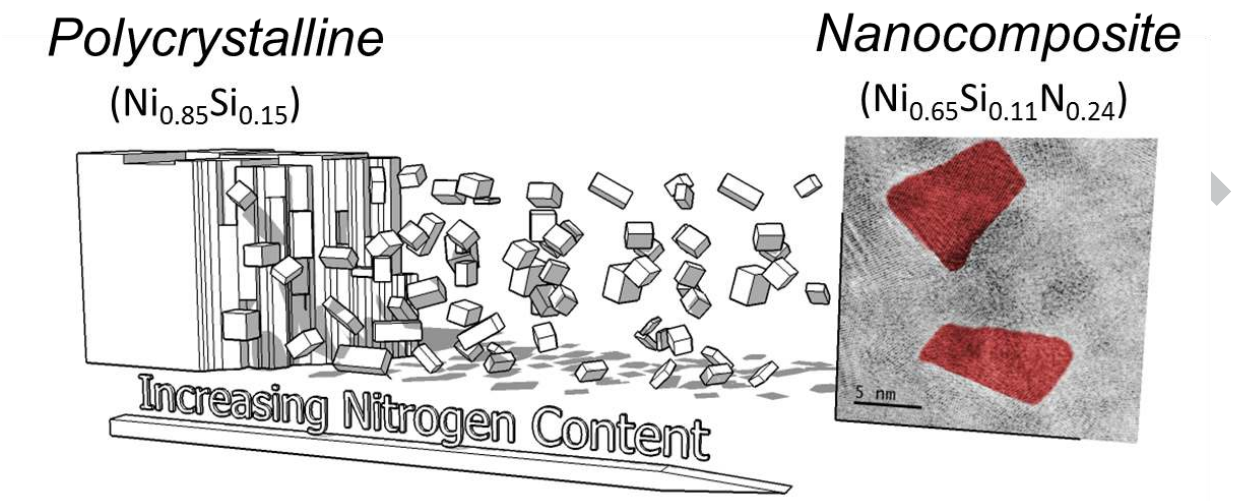

Highlights:

- Deposition of Ni_xSi nanocrystals embedded in SiN_x matrix by HiPIMS without any intentional heating
- Spontaneous formation of Ni_xSi nanocrystals and SiN is occurring with N_2 addition during deposition
- The phase separation relies on a higher chemical affinity of N with Si